Gland Segmentation in Colon Histology Images: The GlaS Challenge Contest

Korsuk Sirinukunwattana[*1], Josien P. W. Pluim[2], Hao Chen[3], Xiaojuan Qi[3], Pheng-Ann Heng[3], Yun Bo Guo[4], Li Yang Wang[4], Bogdan J. Matuszewski[4], Elia Bruni[5], Urko Sanchez[5], Anton Böhm[6], Olaf Ronneberger[6,7], Bassem Ben Cheikh[8], Daniel Racoceanu[8], Philipp Kainz[9,10], Michael Pfeiffer[10], Martin Urschler[11,12], David R. J. Snead[13], and Nasir M. Rajpoot[†‡1]

[1]Department of Computer Science, University of Warwick, Coventry, UK, CV4 7AL
[2]Department of Biomedical Engineering, Eindhoven University of Technology, Eindhoven, Netherlands
[3]Department of Computer Science and Engineering, The Chinese University of Hong Kong.
[4]School of Engineering, University of Central Lancashire, Preston, UK
[5]ExB Research and Development
[6]Computer Science Department, University of Freiburg, Germany
[7]BIOSS Centre for Biological Signalling Studies, University of Freiburg, Germany and Google-DeepMind, London, UK
[8]Sorbonne Universités, UPMC Univ Paris 06, CNRS, INSERM, Biomedical Imaging Laboratory (LIB), Paris, France
[9]Institute of Biophysics, Center for Physiological Medicine, Medical University of Graz, Graz, Austria
[10]Institute of Neuroinformatics, University of Zurich and ETH Zurich, Zurich, Switzerland
[11]Institute for Computer Graphics and Vision, BioTechMed, Graz University of Technology, Graz, Austria
[12]Ludwig Boltzmann Institute for Clinical Forensic Imaging, Graz, Austria
[13]Department of Pathology, University Hospitals Coventry and Warwickshire, Walsgrave, Coventry, CV2 2DX, UK

arXiv:1603.00275v1 [cs.CV] 1 Mar 2016

[*]k.sirinukunwattana@warwick.ac.uk

[†]n.m.rajpoot@warwick.ac.uk

[‡]corresponding author

1

Abstract

Colorectal adenocarcinoma originating in intestinal glandular structures is the most common form of colon cancer. In clinical practice, the morphology of intestinal glands, including architectural appearance and glandular formation, is used by pathologists to inform prognosis and plan the treatment of individual patients. However, achieving good inter-observer as well as intra-observer reproducibility of cancer grading is still a major challenge in modern pathology. An automated approach which quantifies the morphology of glands is a solution to the problem.

This paper provides an overview to the Gland Segmentation in Colon Histology Images Challenge Contest (GlaS) held at MICCAI'2015. Details of the challenge, including organization, dataset and evaluation criteria, are presented, along with the method descriptions and evaluation results from the top performing methods.

Index terms — Histology Image Analysis, Segmentation, Colon Cancer, Intestinal Gland, Digital Pathology

1 Introduction

Glands are important histological structures that are present in most organ systems as the main mechanism for secreting proteins and carbohydrates. A colonic crypt, an intestinal gland found in the epithelial layer of the colon, is made up of a single sheet of columnar epithelium, forming a finger-like tubular structure that extends from the inner surface of the colon into the underlying connective tissue [Rubin et al., 2008, Humphries and Wright, 2008]. There are millions of glands in the human colon. Intestinal glands are responsible for absorption of water and nutrients, secretion of mucus to protect the epithelium from a hostile chemical and mechanical environment [Gibson et al., 1996], as well as being a niche for epithelial cells to regenerate [Shanmugathasan and Jothy, 2000, Humphries and Wright, 2008]. The loss of integrity in cell proliferation, through a mechanism that is not yet clearly understood, results in colorectal adenocarcinoma, the most common type of colon cancer.

The morphology of intestinal glands, including architectural appearance and gland formation, is one of the primary features used in clinical practice to inform prognosis and plan the treatment of individual patients [Compton, 2000, Bosman et al., 2010, Washington et al., 2009]. The differentiation grade of the tumor is based on morphological assessment. Some recent studies indicate that differentiation is an important prognostic factor, and poorly differentiated colorectal adenocarcinoma is associated with nodal metastasis. [Fleming et al., 2012, Loughrey et al., 2014]. Achieving good reproducibility in grading any type of cancer remains one of the challenges in modern pathology. Automated image analysis extracts from histology images a set of numerical features representing the glandular morphology. This approach could increase the effectiveness of cancer grading. To obtain reliable morphological statistics, accurate segmentation of glands is often a crucial step.

The Gland Segmentation in Colon Histology Images (GlaS) challenge[1] brought together computer vision and medical image computing researchers to solve the problem of gland segmentation in digitized images of Hematoxylin and Eosin (H&E) stained tissue slides. Participants developed gland segmentation algorithms, which were applied to benign tissue and to colonic carcinomas. A training dataset was provided, together with ground truth annotations by an expert pathologist. The participants developed and

---

[1] http://www.warwick.ac.uk/bialab/GlaScontest

optimized their algorithms on this dataset. The results were judged on the performance of the algorithms on test datasets. Success was measured by how closely the automated segmentation matched the pathologist's.

2   Related Work

Recent papers [Wu et al., 2005a,b, Gunduz-Demir et al., 2010, Fu et al., 2014, Sirinukunwattana et al., 2015, Cohen et al., 2015] indicate the increasing interest in histology image analysis applied to intestinal gland segmentation. In this section, we review some of these methods.

Wu et al. [2005a] presented a region growing method, which first thresholds an image, in order to separate nuclei from other tissue components. Large empty regions, which potentially correspond to lumen found in the middle of glands, are then used to initialize the seed points for region growing. The expanding process for each seed is terminated when a surrounding chain of epithelial nuclei is reached, and subsequently false regions are removed. As a result of the assumption that a regular gland is always enclosed by an epithelial boundary that has only small gaps between neighboring epithelial nuclei, this algorithm is inevitably susceptible to malformed and incomplete glands, and to various artefacts arising from the tissue preparation process.

In contrast to the above method, which mainly uses pixel-level information, Gunduz-Demir et al. [2010] represented each tissue component as a disk. Each disk is represented by a vertex of a graph, with nearby disks joined by an edge between the corresponding vertices. They proposed an algorithm, using graph connectivity to identify initial seeds for region growing. To avoid an excessive expansion beyond the glandular region, caused, for example, by large gaps in the surrounding epithelial boundary, edges between nuclear objects are used as a barrier to halt region growing. Those regions that do not show glandular characteristics are eliminated at the last step. Although the methods by Wu et al. [2005a] and Gunduz-Demir et al. [2010] perform well in segmenting healthy and benign glands, they are less applicable to cancer cases, where the morphology of glands can be substantially deformed.

Fu et al. [2014] introduced a segmentation algorithm based on polar coordinates. A neighborhood of each gland and a center chosen inside the gland were considered. Using this center to define polar coordinates, the neighborhood is displayed in (r, θ) coordinates with the r-axis horizontal and the θ-axis vertical. One obtains a vertical strip, periodic with period 2π in the vertical direction. As a result, the closed glandular boundary is transformed into an approximately vertical periodic path, allowing fast inference of the boundary through a conditional random field model. Support vector regression is later deployed to verify whether the estimated boundary corresponds to the true boundary. The algorithm performs well in both benign and malignant cases stained by Hematoxylin and DAB. However, the validation on routine H&E stained images was limited only to healthy cases.

Sirinukunwattana et al. [2015] recently formulated a segmentation approach based on Bayesian inference, which allows prior knowledge of the spatial connectivity and the arrangement of neighboring nuclei on the epithelial boundary to be taken into account. This approach treats each glandular structure as a polygon made of a random number of vertices. The idea is based on the observation that a glandular boundary is formed from closely arranged epithelial nuclei. Connecting edges between these epithelial nuclei gives a polygon that encapsulates the glandular structure. Inference of the polygon is

Table 1: Details of the dataset.

Histologic Grade	Number of Images (Width x Height in Pixels)		
	Training Part	Test Part A	Test Part B
Benign	37 { 1 (574×433); 1 (589×453); 35 (775×522)	33 { 1 (574×433); 4 (589×453); 28 (775×522)	4 (775×522)
Malignant	48 { 1 (567×430); 3 (589×453); 44 (775×522)	27 { 1 (578×433); 2 (581×442); 24 (775×522)	16 (775×522)

made via Reversible-Jump Markov Chain Monte Carlo. The approach shows favorable segmentation results across all histologic grades (except for the undifferentiated grade) of colorectal cancers in H&E stained images. This method is slow but effective.

Most of the works for intestinal gland segmentation have used different datasets and/or criteria to assess their algorithms, making it difficult to objectively compare their performance. This challenge was a first attempt to address the issues of reproducibility and comparability. It was also aimed at speeding up even further the development of algorithms for gland segmentation. Note that none of above methods participated in this competition.

3 Materials

The dataset used in this challenge consists of 165 images derived from 16 H&E stained histological sections of stage T3 or T4 colorectal adenocarcinoma. Each section belongs to a different patient, and sections were processed in the laboratory on different occasions. Thus, the dataset exhibits high inter-subject variability in both stain distribution and tissue architecture. The digitization of these histological sections into whole-slide images (WSIs) was accomplished using a Zeiss MIRAX MIDI Slide Scanner with a pixel resolution of $0.465\mu m$. The WSIs were subsequently rescaled to a pixel resolution of $0.620\mu m$ (equivalent to $20\times$ objective magnification).

A total of 52 visual fields from both malignant and benign areas across the entire set of the WSIs were selected in order to cover as wide a variety of tissue architectures as possible. An expert pathologist (DRJS) then graded each visual field as either 'benign' or 'malignant', according to the overall glandular architecture. The pathologist also delineated the boundary of each individual glandular object on that visual field. We used this manual annotation as ground truth for automatic segmentation. Note that different glandular objects in an image may be part of the same gland. This is because a gland is a 3-dimensional structure that can appear as separated objects on a single tissue section. The visual fields were further separated into smaller, non-overlapping images, whose histologic grades (i.e. benign or malignant) were assigned the same value as the larger visual field. Representative example images of the two grades can be seen in Figure 1. This dataset was also previously used in the gland segmentation study by Sirinukunwattana et al. [2015].

In the challenge, the dataset was separated into **Training Part**, **Test Part A**, and **Test Part B**. A breakdown of the details of the dataset is shown in Table 1. The ground truth as well as the histologic grade which reflects morphology of glandular structures were provided for every image in the Training Part at the time of release. We used Test
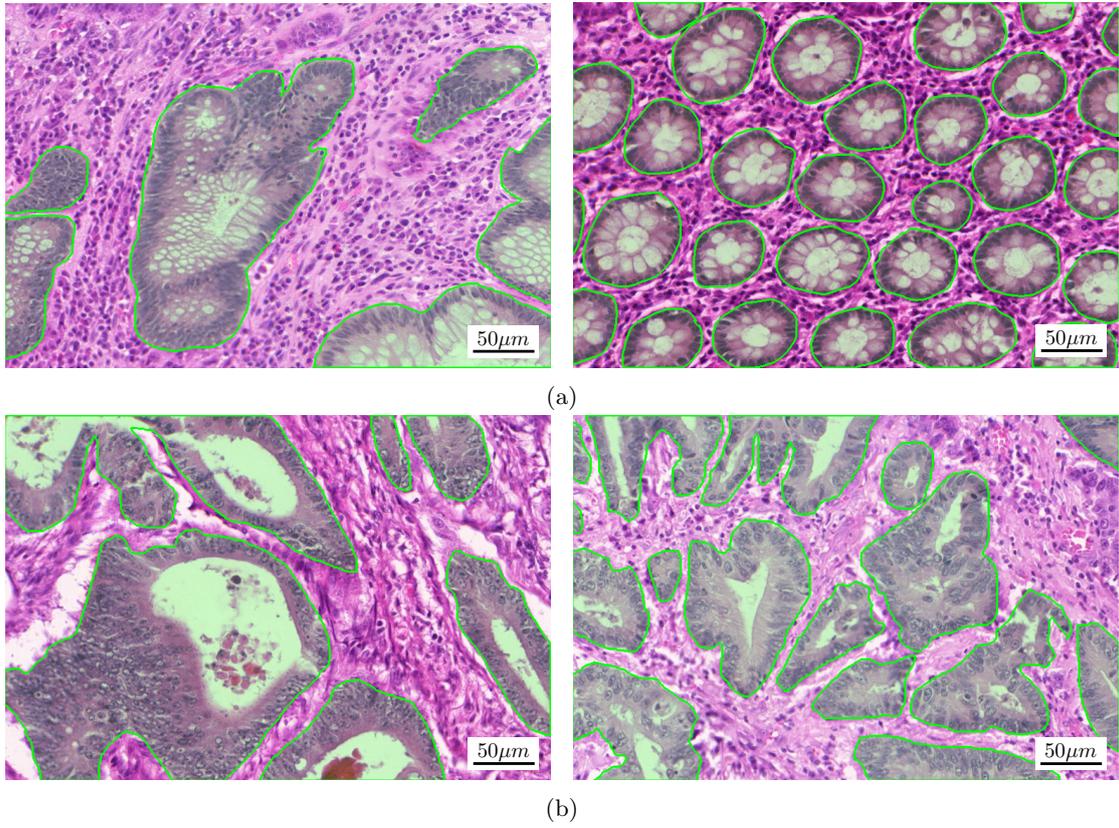
(a)

(b)

Figure 1: Example images of different histologic grades in the dataset: (a) benign and (b) malignant.

Part A and Test Part B as off-site and on-site test datasets respectively. Furthermore, to ensure blindness of evaluation, the ground truth and histologic grade of each image in the test parts were not released to the participants.

4   Challenge Organization

The GlaS challenge contest was officially launched by the co-organizers (KS, JPWP, DRJS, NMR) on April 21st, 2015, and was widely publicized through several channels. At the same point, a challenge website[2] was set up to disseminate challenge-related information and to serve as a site for registration, submission of results, and communication between the organizers and contestants. The challenge involved 4 stages, as detailed below:

Stage 1: Registration and Release of the Training Data   The registration was open for a period of about two months (April 21st to June 30th, 2015). Interested individuals or groups of up to 3 people that were affiliated with an academic institute or an industrial organization could register and download the training data (Training Part, see Section 3 for details) to start developing their gland segmentation algorithms. From this point forward, we will refer to a separate individual or a group of registrants as a 'team'.

Stage 2: Submission of a Short Paper   In order to gain access to the first part of the test data, each registered team was required to submit a 2-page document containing a general description of their segmentation algorithms and some preliminary results obtained from running each algorithm on the training data. Each team could submit up to 3 different methods. The intention of this requirement was for the organizers to identify teams who were serious about participating in the challenge. The organizers based their reviews on two criteria: clarity of the method description and soundness of the validation strategy. Segmentation performance was not considered in this review. The submission of this document was due by July 17th, 2015.

Stage 3: Release of the Test Data Part A and Submission of Segmentation Results   The first part of the test data (Test Part A, see Section 3 for details) was released on August 14th, 2015 to those teams selected from the previous stage which also agreed to participate in the GlaS contest. The teams were given a month to further adjust and optimize their segmentation algorithms, and carry out segmentation on Part A of the test data. Each team could hand-in up to 3 sets of results per method submitted in Stage 2. The submission of the segmentation results was due by September 14th, 2015. Evaluation of the submitted results was not disclosed to the teams until after the challenge event.

Stage 4: GlaS'2015 Challenge Event   The event was held in conjunction with MICCAI'2015 on October 5th, 2015. All teams were asked to produce segmentation results on the second part of the test data (Test Part B, see Section 3) within 45 minutes. The teams could either bring their own machines or conduct an experiment remotely. There was no restriction on the number of machines that the teams could use to produce

---

[2]http://www.warwick.ac.uk/bialab/GlaScontest

results. Those teams that could not be present at the event provided implementations of their algorithms with which the organizers carried out the segmentation on their behalf. Each team was also asked to give a short presentation, discussing their work. At the end of the event, the complete evaluation of segmentation results across both parts of the test data was announced, which included a final ranking of the submitted methods. This information is also available on the challenge website.

4.1 Challenge Statistics

By the end of Stage 1, a total of 110 teams from different academic and industrial institutes had registered. A total of 21 teams submitted the 2-page document for review in Stage 2, and 20 teams were invited to participate in the GlaS competition event. In Stage 3, only 13 teams submitted results on Part A of the test data in time. Late entries were neither evaluated nor considered in the next stage of the competition. On the day of the challenge event, 11 of the 13 teams that submitted the results on time in Stage 3 attended the on-site competition and presented their work. The organizers carried out the segmentation on behalf of the other two teams that could not be present.

5 Evaluation

The performance of each segmentation algorithm was evaluated based on three criteria: 1) accuracy of the detection of individual glands; 2) accuracy of the segmentation of individual glands; and 3) shape similarity between glands and their corresponding segmentation. It may seem that segmentation accuracy would entail shape similarity between a gland and its segmentation. However, in practice, this is not always the case. The metric for segmentation accuracy used in this challenge, was defined and calculated using the label that the algorithm had assigned to each pixel, but the metric for shape similarity used the position assigned by the algorithm to the boundary of each gland. Pixels labels may be fairly accurate, while the boundary curves are very different. The remainder of this section describes all metrics employed in the evaluation.

We use the concept of a pair of corresponding segmented and ground truth objects as proposed in Sirinukunwattana et al. [2015]. Let $\mathcal{S}$ denote a set of all segmented objects and $\mathcal{G}$ denote a set of all ground truth objects. We also include in each of these sets the empty object $\emptyset$. We define a function $G_* : \mathcal{S} \to \mathcal{G}$, by setting, for each segmented object $S \in \mathcal{S}$, $G_*(S) = G \in \mathcal{G}$ where G has the largest possible overlapping area with S. Although there could be more than one $G \in \mathcal{G}$ that maximally overlaps S, this in practice is extremely rare, and it is good enough to consider one of these G as the value of $G_*(S)$. If there is no overlapping G, we set $G_*(S) = \emptyset$. (However, in the context of Hausdorff distance – see Section 5.3 – G_* will be extended in a different way.) Similarly, we define $S_* : \mathcal{G} \to \mathcal{S}$, by setting, for each $G \in \mathcal{G}$, $S_*(G) = S \in \mathcal{S}$, where S has the largest possible overlapping area with G. Note that G_* and S_* are, in general, neither injective, nor surjective. Nor are they inverse to each other, in general. They do, however, assign to each G an $S = S_*(G)$, and to each S a $G = G_*(S)$.

5.1 Detection Accuracy

The F1 score is employed to measure the detection accuracy of individual glandular objects. A segmented glandular object that intersects with at least 50% of its ground truth object is counted as true positive, otherwise it is counted as false positive. A

ground truth glandular object that has no corresponding segmented object or has less than 50% of its area overlapped by its corresponding segmented object is considered as false negative. Given these definitions, the F1 score is defined by

$$\text{F1score} = \frac{2 \cdot \text{Precision} \cdot \text{Recall}}{\text{Precision} + \text{Recall}}, \tag{1}$$

where

$$\text{Precision} = \frac{\text{TP}}{\text{TP} + \text{FP}}, \quad \text{Recall} = \frac{\text{TP}}{\text{TP} + \text{FN}}, \tag{2}$$

and TP, FP, and FN denote respectively the number of true positives, false positives, and false negatives from all images in the dataset.

5.2 Segmentation Accuracy

5.2.1 Object-Level Dice Index

The Dice index [Dice, 1945] is a measure of agreement or similarity between two sets of samples. Given G, a set of pixels belonging to a ground truth object, and S, a set of pixels belonging to a segmented object, the Dice index is defined as follows:

$$\text{Dice}(G, S) = \frac{2|G \cap S|}{|G| + |S|}, \tag{3}$$

where $|\cdot|$ denotes set cardinality. The index ranges over the interval $[0, 1]$, where the higher the value, the more concordant the segmentation result and the ground truth. A Dice index of 1 implies a perfect agreement. It is conventional that the segmentation accuracy on an image is calculated by $\text{Dice}(G_{\text{all}}, S_{\text{all}})$, where G_{all} denotes the set of pixels of all ground truth objects and S_{all} denotes the set of pixels of all segmented objects. The calculation made in this way measures the segmentation accuracy only at the pixel level, not at the gland level, which was the main focus of the competition.

To take the notion of an individual gland into account, we employ the object-level Dice index [Sirinukunwattana et al., 2015]. Let $n_{\mathcal{G}}$ be the number of non-empty ground truth glands, as annotated by the expert pathologist. Similarly let $n_{\mathcal{S}}$ be the number of glands segmented by the algorithm, that is the number of non-empty segmented objects. Let $G_i \in \mathcal{G}$ denote the ith ground truth object, and let $S_j \in \mathcal{S}$ denote the jth segmented object. The object-level Dice index is defined as

$$\text{Dice}_{\text{obj}}(\mathcal{G}, \mathcal{S}) = \frac{1}{2} \left[\sum_{i=1}^{n_{\mathcal{G}}} \gamma_i \text{Dice}(G_i, S_*(G_i)) + \sum_{j=1}^{n_{\mathcal{S}}} \sigma_j \text{Dice}(G_*(S_j), S_j) \right], \tag{4}$$

where

$$\gamma_i = |G_i| / \sum_{p=1}^{n_{\mathcal{G}}} |G_p|, \quad \sigma_j = |S_j| / \sum_{q=1}^{n_{\mathcal{S}}} |S_q| \tag{5}$$

On the right hand side of (4), the first summation term reflects how well each ground truth object overlaps its segmented object, and the second summation term reflects how well each segmented object overlaps its ground truth objects. Each term is weighted by the relative area of the object, giving less emphasis to small segmented and small ground truth objects.

In the competition, the object-level Dice index of the whole test dataset was calculated by including all the ground truth objects from all images in $\mathcal{G}$ and all the segmented objects from all images in $\mathcal{S}$.

5.2.2 Adjusted Rand Index

We also included the adjusted Rand index [Hubert and Arabie, 1985] as another evaluation measure of segmentation accuracy. This index was used for additional assessment of the algorithm performance in Section 8.3.

The adjusted Rand index measures similarity between the set of all ground truth objects $\mathcal{G}$ and the set of all segmented objects $\mathcal{S}$, based on how pixels in a pair are labeled. Two possible scenarios for the pair to be concordant are that (i) they are placed in the same ground truth object in $\mathcal{G}$ and the same segmented object in $\mathcal{S}$, and (ii) they are placed in different ground truth objects in $\mathcal{G}$ and in different segmented objects in $\mathcal{S}$. Define n_{ij} as the number of pixels that are common to both the ith ground truth object and the jth segmented object, $n_{i,\cdot}$ as the total number of pixels in the ith ground truth object, $n_{\cdot,j}$ as the total number of pixels in the jth segmented object, and n as the total number of pixels. Following a simple manipulation, it can be shown that the probability of agreement is equal to

$$P_{\text{agreement}} = \left[\binom{n}{2} + 2 \sum_{i=1}^{n_{\mathcal{G}}} \sum_{j=1}^{n_{\mathcal{S}}} \binom{n_{ij}}{2} - \sum_{i=1}^{n_{\mathcal{G}}} \binom{n_{i,\cdot}}{2} - \sum_{j=1}^{n_{\mathcal{S}}} \binom{n_{\cdot,j}}{2} \right] \Bigg/ \binom{n}{2}. \quad (6)$$

Here, the numerator term corresponds to the total number of agreements, while the denominator term corresponds to the total number of all possible pairs of pixels. Under the assumption that the partition of pixels into ground truth objects in $\mathcal{G}$ and segmented objects in $\mathcal{S}$ follows a generalized hypergeometric distribution, the adjusted Rand index can be formulated as

$$\text{ARI}(\mathcal{G}, \mathcal{S}) = \frac{\sum_{i=1}^{n_{\mathcal{G}}} \sum_{j=1}^{n_{\mathcal{S}}} \binom{n_{i,j}}{2} - \sum_{i=1}^{n_{\mathcal{G}}} \binom{n_i}{2} \sum_{j=1}^{n_{\mathcal{S}}} \binom{n_{\cdot,j}}{2} \Big/ \binom{n}{2}}{\frac{1}{2} \left[\sum_{i=1}^{n_{\mathcal{G}}} \binom{n_{i,\cdot}}{2} + \sum_{j=1}^{n_{\mathcal{S}}} \binom{n_{\cdot,j}}{2} \right] - \sum_{i=1}^{n_{\mathcal{G}}} \binom{n_{i,\cdot}}{2} \sum_{j=1}^{n_{\mathcal{S}}} \binom{n_{\cdot,j}}{2} \Big/ \binom{n}{2}}. \quad (7)$$

The adjusted Rand index is bounded above by 1, and it can be negative.

5.3 Shape Similarity

We measure the shape similarity between the segmented objects in $\mathcal{S}$ and the ground truth objects in $\mathcal{G}$ using the object-level Hausdorff distance. The usual definition of a Hausdorff distance between ground truth object G and segmented object S is

$$\text{H}(G, S) = \max\{\sup_{x \in G} \inf_{y \in S} d(x, y), \sup_{y \in S} \inf_{x \in G} d(x, y)\} \quad (8)$$

where $d(x, y)$ denotes the distance between pixels $x \in G$ and $y \in S$. In this work, we use the Euclidean distance. According to (8), Hausdorff distance is the most extreme value from all distances between the pairs of nearest pixels on the boundaries of S and G. Thus, the smaller the value of the Hausdorff distance, the higher the similarity between the shapes of S and G, and $S = G$ if their Hausdorff distance is zero.

To calculate the overall shape similarity between a pair of corresponding segmented and ground truth objects, we now introduce object-level Hausdorff distance by imitating the definition of object-level Dice index (4). The object-level Hausdorff distance is defined as

$$\text{H}_{\text{obj}}(\mathcal{G}, \mathcal{S}) = \frac{1}{2} \left[\sum_{i=1}^{n_{\mathcal{G}}} \gamma_i \text{H}(G_i, S_*(G_i)) + \sum_{j=1}^{n_{\mathcal{S}}} \sigma_j \text{H}(G_*(S_j), S_j) \right], \quad (9)$$

where the meaning of the mathematical notation is similar to that given in Section 5.2.1. In case a ground truth object G does not have a corresponding segmented object (i.e. $S_*(G) = \emptyset$), the Hausdorff distance is calculated between G and the nearest segmented object $S \in \mathcal{S}$ to G (in the Hausdorff distance) in that image instead. The same applies for a segmented object that does not have a corresponding ground truth object.

6   Ranking Scheme

Each submitted entry was assigned one ranking score per evaluation metric and set of test data. Since there were 3 evaluation metrics (F1 score for gland detection, object-level Dice index for segmentation accuracy, and object-level Hausdorff index for shape similarity) and 2 sets of test data, the total number of ranking scores was 6. The best performing entry was assigned ranking score 1, the second best was assigned ranking score 2, and so on. In care of a tie, the standard competition ranking was applied. For instance, F1 score 0.8, 0.7, 0.7, and 0.6 would result in the ranking scores 1, 2, 2, and 4. The final ranking was then obtained by adding all 6 ranking scores (rank sum). The entry with smallest sum was placed top in the final ranking.

7   Methods

The top ranking methods are described in this section. They are selected from the total of 13 methods that participated in all stages of the challenge. The cut-off for the inclusion in this section was made where there was a substantial gap in the rank sums (see A, Figure 3). Of the 7 selected methods, only 6 preferred to have their methods described here.

7.1   CUMedVision[3]

A novel deep contour-aware network was presented. This method explored the multi-level feature representations with fully convolutional networks (FCN) [Long et al., 2015]. The network outputted segmentation probability maps and depicted the contours of gland objects simultaneously. The network architecture consisted of two parts: a down-sampling path and an up-sampling path. The down-sampling path contained convolutional and max-pooling layers while the up-sampling path contained convolutional and up-sampling layers, which increased the resolutions of feature maps and outputted the prediction masks. In total, there were 5 max-pooling layers and 3 up-sampling layers. Each layer with learned parameters was followed by a non-linear mapping layer (element-wise rectified linear activation).

In order to separate touching glands, the feature maps from hierarchical layers were up-sampled with two different branches to output the segmented object and contour masks respectively. The parameters of the down-sampling path were shared and updated for these two kinds of masks. This could be viewed as a multi-task learning framework with feature representations, simultaneously encoding the information of segmented objects and contours. To alleviate the problem of insufficient training data [Chen et al., 2015], an off-the-shelf model from DeepLab [Chen et al., 2014], trained on the 2012 PASCAL VOC dataset[4], was used to initialize the weights for layers in the

---

[3]Department of Computer Science and Engineering, The Chinese University of Hong Kong.
[4]http://host.robots.ox.ac.uk:8080/pascal/VOC/voc2012/index.html

down-sampling path. The parameters of the network were obtained by minimizing the loss function with standard back-propagation [5].

The team submitted two entries for evaluation. **CUMedVision1** was produced by FCN with multi-level feature representations relying only on gland object masks, while **CUMedVision2** was the results of the deep contour-aware network, which considers gland object and contour masks simultaneously.

7.2 CVML[6]

In the first, preprocessing, stage the images were corrected to compensate for variations in the appearance due to a variability of the tissue staining process. This was implemented through histogram matching, where the target histogram was calculated from the whole training data, and the individual image histograms were used as inputs. The main processing stage was based on two methods: a convolutional neural network (CNN) [Krizhevsky et al., 2012] for a supervised pixel classification, and a level set segmentation for grouping pixels into spatially coherent structures. The employed CNN used an architecture with two convolutional, pooling and fully connected layers. The network was trained with three target classes. The classes were designed to represent (1) the tubular interior of the glandular structure (inner class), (2) epithelial cells forming boundary of the glandular structure (boundary class) and (3) inter-gland tissue (outer class). The inputs to the CNN were 19×19 pixel patches sliding across the adjusted RGB input image. The two convolutional layers used 6×6 and 4×4 kernels with 16 and 36 feature maps respectively. The pooling layers, implementing the mean function, used 2×2 receptive fields and 2×2 stride. The first and second fully connected layers used the rectified linear unit and softmax functions respectively. The outputs from the CNN were two probability maps representing the probability of each image pixel belonging to the inner and boundary classes. These two probability maps were normalized between -1 and 1 and used as a propagation term, along with an advection term and a curvature flow term. These terms were part of the hybrid level set model described in Zhang et al. [2008]. In the post-processing stage, a sequence of morphological operations was performed to removed small objects, fill holes and disconnect weakly connected objects. Additionally, if an image boundary intersecting an object forms a hole, the corresponding pixels was labeled as part of that object. The team submitted a single entry for evaluation, henceforth referred to as **CVML**.

7.3 ExB[7]

This method first preprocessed the data by performing per channel zero mean and unit variance normalization, where the mean and variance were computed from the training data. The method then exploited the local invariance properties of the task by applying a set of transformations to the data. At training time, the dataset was augmented by applying affine transformations, Gaussian blur and warping. During testing, both image mirroring and rotation were applied.

The main segmentation algorithm consisted of a multi-path convolutional neural network. Each path was equipped with a different set of convolutional layers and configured

---

[5]More details will be available at: `http://www.cse.cuhk.edu.hk/~hchen/research/2015miccai_gland.html`

[6]School of Engineering, University of Central Lancashire, Preston, UK.

[7]ExB Research and Development.

to capture features from different views in a local-global fashion. All the different paths were connected to a set of two fully connected layers. A leaky rectified linear unit was used as a default activation function between layers, and a softmax layer was used after the last fully connected layer. Every network was trained via stochastic gradient descent with momentum, using a step-wise learning rate schedule [Krizhevsky et al., 2012]. The network was randomly initialized such that unit variance was preserved across layers. It was found that using more than three paths led to heavy over-fitting – this was due to insufficient training data.

Simple-path networks were trained to detect borders of glands. The ground truth for these networks was constructed using a band of width $K \in [5, 10]$ pixels along a real gland border. These values of K were found to produce optimal and equivalent quantitative results, measured by the F1 score and the object-Dice index. The output of these networks was used to better calibrate the final prediction.

In the post-processing step, a simple method was applied to clean noise and fill holes in the structures. Thresholding was applied to remove spurious structures with diameter smaller than a certain epsilon. Filling-hole criteria based on diameter size was also used.

Using the initial class discrimination (benign and malignant), a simple binary classifier constructed from a convolutional neural network with 2 convolutional and 1 fully connected layers was trained. This binary classifier used the raw image pixels as input. The output of the classifier was used together with the border networks and the post-processing method to apply a different set of parameters/thresholds depending on the predicted class. The hyperparameters for the entire pipeline, including post-processing and border networks, were obtained through cross-validation.

For this method, the team submitted 3 entries. **ExB 1** was a two-path network including both the border network for detecting borders of glands and the binary classification to differentiate between the post-processing parameters. **ExB 2** was similar to ExB 1 without the use of the border network. **ExB 3** used a two-path network without any post-processing.

7.4   Image Analysis Lab Uni Freiburg[8]

The authors applied a u-shaped deep convolutional network "u-net"[9] [Ronneberger et al., 2015] for the segmentation. The input was the raw RGB image and the output was a binary segmentation map (glands and background). The network consisted of an analysis-path constructed from a sequence of convolutional layers and max-pooling layers, followed by a synthesis path with a sequence of up-convolutional layers and convolutional layers, resulting in 23 layers in total. Additional shortcut-connections propagated the feature maps at all detail levels from the analysis to the synthesis path. The network was trained from scratch in an end-to-end fashion with only the images and ground truth segmentation maps provided by the challenge organizers. To teach the network the desired invariances and to avoid overfitting, the training data were augmented with randomly transformed images and the correspondingly transformed segmentation maps. The applied transformations were random elastic deformations, rotations, shifts, flips, and blurs. The color transformations were random multiplications applied in the HSV color space. To avoid accidentally joining touching objects, a high pixel-wise loss weight

---

[8]Computer Science Department and BIOSS Centre for Biological Signalling Studies, University of Freiburg, Germany.

[9]The implementation of the u-net is freely available at `http://lmb.informatik.uni-freiburg.de/people/ronneber/u-net/`.

was introduced for pixels in thin gaps between objects in the training dataset (see Ronneberger et al. [2015]). The exact same u-net layout with the same hyperparameters as in Ronneberger et al. [2015] was used for the challenge. The only difference were more training iterations and a slower decay of the learning rate.

The team submitted two entries. The first entry **Freiburg1** was a connected component labelling applied to the raw network output. The second entry **Freiburg2** post-processed the segmentation maps with morphological hole-filling and deletion of segments smaller than 1000 pixels.

7.5 LIB[10]

Intestinal glands were divided according to their appearance into three categories: hollow, bounded, and crowded. A hollow gland was composed of lumen and goblet cells and it could be a hole in the tissue surface. A bounded gland had the same composition, but in addition, it was surrounded by a thick epithelial layer. A crowded gland was composed of bunches of epithelial cells clustered together and it might have shown necrotic debris.

The tissue was first classified into one of the above classes before beginning the segmentation. The classification relied on the characterization of the spatial distribution of cells and the topology of the tissue. Therefore, a closing map was generated with a cumulative sum of morphological closing by a disk of increasing radius (1 to 40 pixels) on the binary image of nuclear objects, which were segmented by the k-means algorithm in the RGB colour space. The topological features were calculated from a normalized closing map in MSER fashion (Maximally Stable Extremal Region, Matas et al. [2004]) as the number of regions below three different thresholds (25%, 50% and 62.5%) and above one threshold (90%), their sizes and the mean of their corresponding values in the closing map. The first three thresholds characterized the holes and the fourth one characterized the thickness of nuclear objects. After classifying the tissue with a Naive Bayes classifier trained on these features, a specific segmentation algorithm was applied.

Three segmentation algorithms were presented, one for each category. Hollow glands were delineated by morphological dilation on regions below 50%. Bounded gland candidates were first detected as hollow glands, then the thickness of nuclear objects surrounding the region was evaluated by generating a girth map and a solidity map [Ben Cheikh et al., 2016], then after classifying nuclear objects, the epithelial layer was added or the candidate was removed. Crowded glands were identified as populous regions (regions above 90%), and then morphological filtering was applied for refinement. The team submitted a single entry labeled as **LIB** for evaluation.

7.6 vision4GlaS[11]

Given an H&E-stained RGB histopathological section, the gland segmentation method was based on a pixel-wise classification and an active contour model, and it proceeded in three steps [Kainz et al., 2015]. In a first preprocessing step the image was rescaled to

---

[10]Sorbonne Universités, UPMC Univ Paris 06, CNRS, INSERM, Biomedical Imaging Laboratory (LIB), Paris, France.

[11]Institute of Biophysics, Center for Physiological Medicine, Medical University of Graz, Graz, Austria; Institute of Neuroinformatics, University of Zurich and ETH Zurich, Zurich, Switzerland; Institute for Computer Graphics and Vision, BioTechMed, Graz University of Technology, Graz, Austria; Ludwig Boltzmann Institute for Clinical Forensic Imaging, Graz, Austria.

half the spatial resolution, and color deconvolution separated the stained tissue components. The red channel of the deconvolved RGB image represented the tissue structure best and was therefore considered for further processing. Next, two convolutional neural networks (CNNs) [LeCun et al., 2010] of seven layers each were trained for pixel-wise classification on a set of image patches. Each network was trained with ReLU nonlinearities, and stochastic gradient descent with momentum, weight decay, and dropout regularization to minimize a negative log-likelihood loss function. The first CNN, called Object-Net, was trained to distinguish four classes: (i) benign background, (ii) benign gland, (iii) malignant background, and (iv) malignant gland. For each image patch the probability distribution over the class labels was predicted, using a softmax function. The Object-Net consisted of three convolutional layers followed by max-pooling, a final convolutional layer and three fully connected layers. The second – architecturally similar – CNN called Separator-Net, learned to predict pixels of gland-separating structures in a binary classification task. Ground truth was generated by manually labeling image locations, close to two or more gland borders, as gland-separating structures. In the final step the segmentation result was obtained by combining the outputs of the two CNNs. Predictions for benign and malignant glands were merged, and predictions of gland-separating structures were subtracted to emphasize the foreground probabilities. Background classes were handled similarly. Using these refined foreground and background maps, a figure-ground segmentation based on weighted total variation was employed to find a globally optimal solution. This approach optimized a geodesic active contour energy, which minimized contour length while adhering to the refined CNN predictions [Bresson et al., 2007]. The team submitted a single entry, referred to as **vision4GlaS**.

8 Results and Discussion

8.1 Summary of the Methods

The methods described above take one of the following two approaches to segmentation: (a) they start by identifying pixels corresponding to glands which are then grouped together to form separated, spatially coherent objects; (b) they begin with candidate objects that are then classified as glands or non-glands. All methods that are based on CNNs (CUMedVision, CVML, ExB, Freiburg, and vision4GlaS) follow the former approach. CVML, ExB, and vision4GlaS built CNN classifiers that assign a gland-related or non-gland-related label to every pixel in an image, by taking patch(es) centered at the pixel as input. ExB, in particular, use multi-path networks into which patches at different sizes are fed, in order to capture contextual information at multiple scales. CUMedVision and Freiburg, on the other hand, base their pixel classifier on a fully convolutional network architecture [Long et al., 2015], allowing simultaneous pixel-wise label assignment at multiple pixel locations. To separate gland-related pixels into individual objects, CVML and vision4GlaS deploy contour based approaches. ExB trains additional networks for glandular boundary, while CUMedVision and Freiburg explicitly include terms for boundary in the training loss function of their networks. The only method that follows the latter approach for object segmentation is LIB. In this method, candidate objects forming part of a gland (i.e., lumen, epithelial boundary) are first identified, and then classified into different types, followed by the final step of segmentation.

A variety of data transformation and augmentation were employed to deal with vari-

Table 2: Summary results. The evaluation is carried out according to the challenge criteria described in Section 6. A ranking score is assigned to each algorithm according to its performance in each evaluation measure, obtained from each test part. The entries are listed in a descending order based on their rank sum

Method	F1score				$Dice_{obj}$				H_{obj}				Rank Sum
	Part A		Part B		Part A		Part B		Part A		Part B		
	Score	Rank	Score	Rank	Score	Rank	Score	Rank	Score	Rank	Score	Rank	
CUMedVision2	0.912	1	0.716	3	0.897	1	0.781	5	45.418	1	160.347	6	17
ExB1	0.891	4	0.703	4	0.882	4	0.786	2	57.413	6	145.575	1	21
ExB3	0.896	2	0.719	2	0.886	2	0.765	6	57.350	5	159.873	5	22
Freiburg2	0.870	5	0.695	5	0.876	5	0.786	3	57.093	3	148.463	3	24
CUMedVision1	0.868	6	0.769	1	0.867	7	0.800	1	74.596	7	153.646	4	26
ExB2	0.892	3	0.686	6	0.884	3	0.754	7	54.785	2	187.442	8	29
Freiburg1	0.834	7	0.605	7	0.875	6	0.783	4	57.194	4	146.607	2	30
CVML	0.652	9	0.541	8	0.644	10	0.654	8	155.433	10	176.244	7	52
LIB	0.777	8	0.306	10	0.781	8	0.617	9	112.706	9	190.447	9	53
vision4GlaS	0.635	10	0.527	9	0.737	9	0.610	10	107.491	8	210.105	10	56

ation within the data. In order to counter the effect of stain variation, CVML and ExB performed transformations of the RGB color channels, vision4GlaS used a stain deconvolution technique to obtain only the basophilic channel in their preprocessing step. By contrast, Freiburg tackled the issue of stain variability through data augmentation, which implicitly forces the networks to be robust to stain variation to some extent. As is common among methods using CNNs, spatial transformations, such as affine transformations (e.g. translation, rotation, flip), elastic deformations (e.g. pincushion and barrel distortions), and blurring, were also used in the data augmentation to teach the network to learn features that are spatially invariant. The other benefit of data augmentation is it provides, to some extent, avoidance of over-fitting.

ExB, LIB, and vision4GlaS incorporated histologic grades of glands in their segmentation approach. In ExB, procedures and/or parameter values used in boundary detection and post-precessing steps were different, subject to the predicted histologic grade of an image. vision4GlaS classified pixels based on histological information. Although not explicit, LIB categorized candidate objects forming glands according to their appearance, related to histologic grades, before treating them in different ways.

As a post-processing step, many segmentation algorithms employed simple criteria and/or a sequence of morphological operations to improve their segmentation results. A common treatment was to eliminate small spurious segmented objects. Imperfections in pixel labelling can result in the appearance of one or more holes in the middle of an object. Filling such holes is often necessary. In addition to these operations, CVML performed morphological operations to separate accidentally joined objects.

8.2 Evaluation Results

Table 2 summarizes the overall evaluation scores and ranks achieved by each entry from each test part. We list the entries according to the order of their rank sum, which indicates the overall performance across evaluation measures and tasks of the entries. The lower the rank sum, the more favorable the performance. The top three entries according to the overall rank sum in descending order are CUMedVision2, ExB1, and
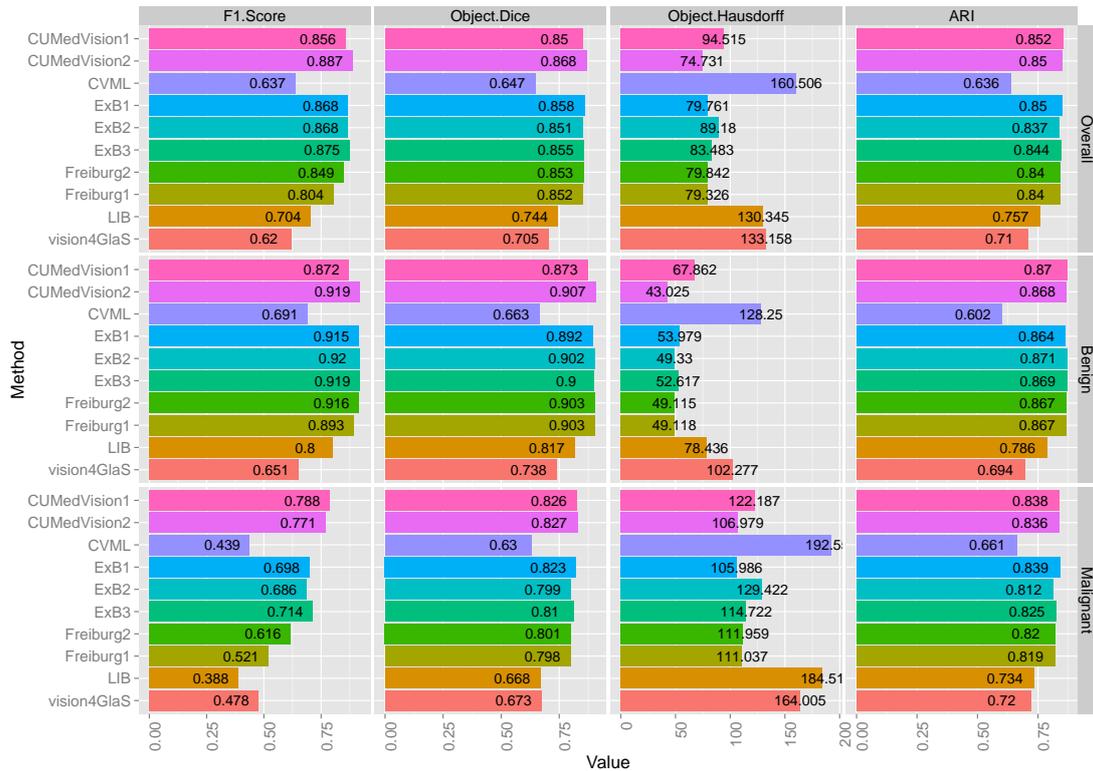
Figure 2: Performance scores achieved by different entries on the combined test data. Evaluation is conducted on three subsets of the data: (1st row) the whole test data, (2nd row) benign, and (3rd row) malignant.

		F1.Score	Object.Dice	Object.Hausdorff	ARI
Overall	CUMedVision1	0.856	0.85	94.515	0.852
	CUMedVision2	0.887	0.868	74.731	0.85
	CVML	0.637	0.647	160.506	0.636
	ExB1	0.868	0.858	79.761	0.85
	ExB2	0.868	0.851	89.18	0.837
	ExB3	0.875	0.855	83.483	0.844
	Freiburg2	0.849	0.853	79.842	0.84
	Freiburg1	0.804	0.852	79.326	0.84
	LIB	0.704	0.744	130.345	0.757
	vision4GlaS	0.62	0.705	133.158	0.71
Benign	CUMedVision1	0.872	0.873	67.862	0.87
	CUMedVision2	0.919	0.907	43.025	0.868
	CVML	0.691	0.663	128.25	0.602
	ExB1	0.915	0.892	53.979	0.864
	ExB2	0.92	0.902	49.33	0.871
	ExB3	0.919	0.9	52.617	0.869
	Freiburg2	0.916	0.903	49.115	0.867
	Freiburg1	0.893	0.903	49.118	0.867
	LIB	0.8	0.817	78.436	0.786
	vision4GlaS	0.651	0.738	102.277	0.694
Malignant	CUMedVision1	0.788	0.826	122.187	0.838
	CUMedVision2	0.771	0.827	106.979	0.836
	CVML	0.439	0.63	192.5	0.661
	ExB1	0.698	0.823	105.986	0.839
	ExB2	0.686	0.799	129.422	0.812
	ExB3	0.714	0.81	114.722	0.825
	Freiburg2	0.616	0.801	111.959	0.82
	Freiburg1	0.521	0.798	111.037	0.819
	LIB	0.388	0.668	184.51	0.734
	vision4GlaS	0.478	0.673	164.005	0.72

ExB3. However, if rank sum is considered with respect to the test part, the three best entries are CUMedVision2, ExB2, and ExB3 for part A; whereas in part B, CUMedVision1, ExB1, and Freiburg2 come at the top. A summary of the ranking results from the competition can be found in A.

8.3 Additional Experiments

In the challenge, the split of the test data into two parts – Part A (60 images) for off-site test and Part B (20 images) for on-site test – to some extent introduces bias into the performance evaluation of the segmentation algorithms due to equal weight given to performance on the two test parts. The algorithms that perform particularly well on Test Part B would therefore get a better evaluation score even though they may not have performed as well on Test Part A, where the majority of the test dataset is to be found. In addition, the imbalance between the benign and malignant classes in Test Part B, only 4 benign (20%) and 16 malignant (80%) images, would also favor algorithms that perform well on the malignant class. In order to alleviate these issues, we merged the two test parts and re-evaluated the performance of all the entries. In addition, as suggested by one of the participating teams, the adjusted Rand index is included as another performance measurement for segmentation.

The evaluation scores calculated from the combined two test parts are presented as bar chart in Figure 2. The final rankings based on the rank sums of evaluation scores calculated from the combined two test parts are reported in Table 3. Here,

Table 3: Ranking results of the entries when the two parts of test data are combined. Two set of ranking scheme are considered: a) F1score + Dice_{obj}+H_{obj} and b) F1score + ARI + H_{obj}. In addition to the evaluation on the whole test data (overall), the entries are evaluated on a subset of the data according to the histologic labels, i.e. benign and malignant.

| Entry | Final Ranking | | | | | |
| | F1score + Dice_{obj}+H_{obj} | | | F1score + ARI + H_{obj} | | |
	Overall	Benign	Malignant	Overall	Benign	Malignant
CUMedVision1	7	7	3	4	6	3
CUMedVision2	1	1	1	1	2	2
CVML	10	10	10	10	10	10
ExB1	2	6	2	2	7	1
ExB2	6	3	7	7	1	7
ExB3	3	5	4	3	3	4
Freiburg1	4	4	6	6	5	6
Freiburg2	5	2	5	5	4	5
LIB	8	8	9	8	8	9
vision4GlaS	9	9	8	9	9	8

two set of rank sums are considered: one calculated according to the criteria of the competition (i.e., F1score + Dice_{obj} + H_{obj}), and the other where the adjusted Rand index is used instead of the object-level Dice index to evaluate segmentation accuracy (i.e., F1score + ARI + H_{obj}). For both sets of rank sums, the new ranking orders are largely similar to those reported in Section 8.2, with a few swaps in the order, while the top three entries remaining the same, namely CUMedVision2, ExB1, ExB3.

The main factors that negatively affect the performance of the methods are a number of challenges presented by the dataset. Firstly, large white empty areas corresponding to the lumen of the gastrointestinal tract which are not in the interior of intestinal glands can easily confuse the segmentation algorithms. Secondly, characteristics of non-glandular tissue can sometimes resemble that of the glandular tissue. For instance, connective tissue in muscularis mucosa or sub-mucosa layers of the colon is stained white and pinkish and has less dense nuclei, thus resembling the inner part of glands. In the case where there is less stain contrast between nuclei and cytoplasm due to elevated levels of Hematoxylin stain, non-glandular tissue with dense nuclei can look similar to malignant epithelial tissue. Thirdly, small glandular objects are blended into the surrounding tissue and can be easily mis-detected. A careful inspection of the segmentation results generated by each entry showed that methods by CUMedVision, ExB, and Freiburg better avoid over-segmentation or under-segmentation when facing the above-mentioned pitfalls.

The performance of each entry with respect to the histologic grade of cancer was also examined. Their evaluation scores based on benign and malignant samples are reported in the second and the third rows of Figure 2 respectively, and the ranking orders derived from the rank sums of the scores are shown in Table 3. Based on these results, one can

get a better contrast between the performance of the entries that enforce border separation and those that do not. By applying a predicted border mask to separate clumped segmented objects, CUMedVision2 performs better than CUMedVision1, which tends to produce segmentation results that merge neighboring glands together, in both benign and malignant cases. Similarly, ExB1 is able to segment malignant glands better than ExB2 and ExB3 that do not utilize border separation. However, this can have an adverse effect if the algorithm already yields segmentation results that separate individual objects well, such as in the case of ExB1 which under-segments benign glandular objects as compared to its counterparts ExB2 and ExB3.

8.4 General Discussion

The objectives of this challenge were to raise the research community's awareness of the existence of the intestinal gland segmentation problem in routine stained histology images, and at the same time to provide a platform for a standardized comparison of the performance of automatic and semi-automatic algorithms. The challenge attracted a lot of attention from researchers, as can be seen from the number of registered teams/individuals and the number of submissions at each stage of the competition. Interestingly, some of the teams had no experience in working with histology images before. We would like to emphasize that finding the best performing approach is not the main objective of the competition, but rather pushing the boundaries of the-state-of-the-art approaches. Already, we have seen quite interesting developments from many participating teams and the leading algorithms have produced excellent results, both qualitatively and quantitatively.

As noted in the introduction, morphometric analysis of the appearance of cells and tissues, especially those forming glands from which tumors originate, is one of the key components towards precision medicine, and segmentation is the first step to attain morphological information. Some may have argued that there is no need to perform segmentation, but instead, to follow conventional pattern recognition approaches by extracting mathematical features which normally capture local and/or global tissue architecture and then identifying features that are most suited to the objective of the study. It is true that there are a number of successful works that follow such an approach [Jafari-Khouzani and Soltanian-Zadeh, 2003, Tabesh et al., 2007, Altunbay et al., 2010, Basavanhally et al., 2010, Ozdemir and Gunduz-Demir, 2013, Gultekin et al., 2015]. However, because these extracted features are often physically less interpretable in the eyes of practitioners, it is difficult to adopt such an approach in clinical settings. On the other hand, the appearance of glands such as size and shape obtained through segmentation is easy to interpret. Segmentation also helps to localize other type of information (e.g., texture, spatial arrangement of cells) that is specific to the glandular areas.

Even though the dataset used in the challenge included images of different histologic grades taken from several patients, it lacked other aspects. First of all, inter-observer variability was not taken into account as the ground truth was generated by a single expert. This is because the intricate and arduous nature of the problem makes it difficult to find several volunteer experts to perform manual segmentation. Considerable experience is required in order to delineate boundaries of malignant glands, which are not so well-defined as those of the benign ones. Moreover, a single image can contain a large number of glands to be segmented, making the task very laborious. Secondly, digitization variability was also not considered in this dataset. It is, in fact, very important to evaluate the robustness of algorithms when the data are scanned by different

instruments. As whole-slide scanners are becoming increasingly available, this type of real-world problem should be expected.

The choice of evaluation measures would also affect the comparative results. In this challenge, we emphasized object segmentation and accordingly defined the object-level Dice index and the object-level Hausdorff distance to measure segmentation accuracy at the object level rather than at the pixel level. Nonetheless, it has been suggested that these measures are too strict, as they put a severe penalty on mismatch of the objects. One could replace these measures by less conservative ones, for example, adjusted Rand index [Hubert and Arabie, 1985] or a topology preserving warping error [Jain et al., 2010] for segmentation and elastic distance [Younes, 1998, Joshi et al., 2007] for shape similarity. For this reason, we included adjusted rand index as an alternative to object-level Dice index in Section 8.3. As we have already pointed out, this results in only a minor change in the ranking order of the entries. Another aspect that was not explicitly included in the evaluation was execution times. Nevertheless, all the algorithms were capable of completing the segmentation task on the on-site test data (Part B) in the given amount of time with or without limitation of resources. Time efficiency is required to process large scale data, such as whole-slide images, whose volume is growing by the day as slides are routinely scanned. Still, in medical practice, accuracy is far more important than speed.

The challenge is now completed, but the dataset will remain available for research purposes so as to continually attract newcomers to the problem and to encourage development of state-of-the-art methods. Extension of the dataset to address inter-observer and inter-scanner variability seems to be the most achievable aim in the near future. Beyond the scope of segmentation, there lie various extremely interesting future research directions. Previous studies have shown the strong association between the survival of colorectal cancer patients and tumor-related characteristics, including lymphocytic infiltration [Galon et al., 2006, Fridman et al., 2012], desmoplasia [Tommelein et al., 2015], tumor budding [Mitrovic et al., 2012], and necrosis [Richards et al., 2012]. A systematic analysis of these characteristics with the help of gland segmentation as part of automatic image analysis framework could lead to a better understanding of the relevant cancer biology as well as bring precision and accuracy into assessment and prediction of the outcome of the cancer.

9 Conclusions

This paper presented a summary of the Gland Segmentation in Colon Histology Images (GlaS) Challenge Contest which was held in conjunction with the 18th International Conference on Medical Image Computing and Computer Assisted Interventions (MICCAI'2015). The goal of the challenge was to bring together researchers interested in the gland segmentation problem, to validate the performance of their existing or newly invented algorithms on the same standard dataset. In the final round, the total number of submitted entries for evaluation was 19, and we presented here in this paper 10 of the leading entries. The dataset used in the challenge has been made publicly available and can be accessed at the challenge website (`http://www.warwick.ac.uk/bialab/GlasContest/`). Those who are interested in developing or improving their own approaches are encouraged to use this dataset for quantitative evaluation.

10   Acknowledgements

A   The Complete Contest Results

A summary of the ranking results from the contest is given in Figure 3.

Method	Rank						Sum
	F1 Score		Object Dice		Object Hausdorff		
	Part A	Part B	Part A	Part B	Part A	Part B	
CUMedVision 2	1	3	1	5	1	6	17
ExB 1	4	4	4	2	6	1	21
ExB 3	2	2	2	6	5	5	22
Freiburg 2[a]	5	5	5	3	3	3	24
CUMedVision 1	6	1	8	1	8	4	28
ExB 2	3	6	3	7	2	8	29
Freiburg 1[a]	8	8	6	4	4	2	32
CVIP Dundee[b]	7	7	7	8	7	10	46
CVML	10	9	11	9	11	7	57
LIB	9	17	9	12	9	9	65
vision4GlaS	11	10	10	14	10	11	66
LIST	13	11	14	11	14	14	77
Ching-Wei Wang 1[c]	12	12	15	13	16	16	84
Bioimage Informatics	16	15	17	10	18	12	88
Ching-Wei Wang 2[c]	14	13	16	15	17	17	92
SUTECH	15	18	13	18	13	15	92
ISI Kolkatta	18	16	18	19	12	13	96
FIMM	19	19	12	17	15	19	101
Ching-Wei Wang 3[c]	17	14	19	16	19	18	103

[a] Image Analysis Lab Uni Freiburg: Freiburg 2 = post-processing, Freiburg 1 = raw

[b] CVIP Dundee: feature level fusion

[c] Ching-Wei Wang: Ching-Wei Wang 1 = no preprocess fill hole, Ching-Wei Wang 2 = no preprocess hole, Ching-Wei Wang 3 = preprocess fill hole

Figure 3: The ranking results from the GlaS Challenge Contest.

References

Dogan Altunbay, Celal Cigir, Cenk Sokmensuer, and Cigdem Gunduz-Demir. Color graphs for automated cancer diagnosis and grading. *Biomedical Engineering, IEEE*

Transactions on, 57(3):665–674, 2010.

Ajay Nagesh Basavanhally, Shridar Ganesan, Shannon Agner, James Peter Monaco, Michael D Feldman, John E Tomaszewski, Gyan Bhanot, and Anant Madabhushi. Computerized image-based detection and grading of lymphocytic infiltration in HER2+ breast cancer histopathology. *Biomedical Engineering, IEEE Transactions on*, 57(3):642–653, 2010.

Bassem Ben Cheikh, Philippe Bertheau, and Daniel Racoceanu. A structure-based approach for colon gland segmentation in digital pathology. In *SPIE Medical Imaging*. International Society for Optics and Photonics, 2016.

Fred T Bosman, Fatima Carneiro, Ralph H Hruban, Neil D Theise, et al. *WHO classification of tumours of the digestive system.* Number Ed. 4. World Health Organization, 2010.

Xavier Bresson, Selim Esedolu, Pierre Vandergheynst, Jean-Philippe Thiran, and Stanley Osher. Fast global minimization of the active contour/snake model. *Journal of Mathematical Imaging and Vision*, 28(2):151–167, 2007.

Hao Chen, Qi Dou, Dong Ni, Jie-Zhi Cheng, Jing Qin, Shengli Li, and Pheng-Ann Heng. Automatic fetal ultrasound standard plane detection using knowledge transferred recurrent neural networks. In *Medical Image Computing and Computer-Assisted Intervention–MICCAI 2015*, pages 507–514. Springer, 2015.

Liang-Chieh Chen, George Papandreou, Iasonas Kokkinos, Kevin Murphy, and Alan L Yuille. Semantic image segmentation with deep convolutional nets and fully connected CRFs. *arXiv preprint arXiv:1412.7062*, 2014.

Assaf Cohen, Ehud Rivlin, Ilan Shimshoni, and Edmond Sabo. Memory based active contour algorithm using pixel-level classified images for colon crypt segmentation. *Computerized Medical Imaging and Graphics*, 43:150–164, 2015.

Carolyn C Compton. Updated protocol for the examination of specimens from patients with carcinomas of the colon and rectum, excluding carcinoid tumors, lymphomas, sarcomas, and tumors of the vermiform appendix: a basis for checklists. *Archives of Pathology & Laboratory Medicine*, 124(7):1016–1025, 2000.

Lee R Dice. Measures of the amount of ecologic association between species. *Ecology*, 26(3):297–302, 1945.

Matthew Fleming, Sreelakshmi Ravula, Sergei F Tatishchev, and Hanlin L Wang. Colorectal carcinoma: Pathologic aspects. *Journal of Gastrointestinal Oncology*, 3(3): 153, 2012.

Wolf Herman Fridman, Franck Pagès, Catherine Sautès-Fridman, and Jérôme Galon. The immune contexture in human tumours: impact on clinical outcome. *Nature Reviews Cancer*, 12(4):298–306, 2012.

Hao Fu, Guoping Qiu, Jie Shu, and M. Ilyas. A novel polar space random field model for the detection of glandular structures. *Medical Imaging, IEEE Transactions on*, 33 (3):764–776, March 2014. ISSN 0278-0062. doi: 10.1109/TMI.2013.2296572.

Jérôme Galon, Anne Costes, Fatima Sanchez-Cabo, Amos Kirilovsky, Bernhard Mlecnik, Christine Lagorce-Pagès, Marie Tosolini, Matthieu Camus, Anne Berger, Philippe Wind, et al. Type, density, and location of immune cells within human colorectal tumors predict clinical outcome. *Science*, 313(5795):1960–1964, 2006.

Peter R Gibson, Robert P Anderson, John M Mariadason, and Andrew J Wilson. Protective role of the epithelium of the small intestine and colon. *Inflammatory bowel diseases*, 2(4):279–302, 1996.

Tunc Gultekin, Can Fahrettin Koyuncu, Cenk Sokmensuer, and Cigdem Gunduz-Demir. Two-tier tissue decomposition for histopathological image representation and classification. *Medical Imaging, IEEE Transactions on*, 34(1):275–283, 2015.

Cigdem Gunduz-Demir, Melih Kandemir, Akif Burak Tosun, and Cenk Sokmensuer. Automatic segmentation of colon glands using object-graphs. *Medical Image Analysis*, 14(1):1–12, 2010.

Lawrence Hubert and Phipps Arabie. Comparing partitions. *Journal of Classification*, 2(1):193–218, 1985.

Adam Humphries and Nicholas A Wright. Colonic crypt organization and tumorigenesis. *Nature Reviews Cancer*, 8(6):415–424, 2008.

Kourosh Jafari-Khouzani and Hamid Soltanian-Zadeh. Multiwavelet grading of pathological images of prostate. *Biomedical Engineering, IEEE Transactions on*, 50(6): 697–704, 2003.

Viren Jain, Benjamin Bollmann, Mark Richardson, Daniel R Berger, Moritz N Helmstaedter, Kevin L Briggman, Winfried Denk, Jared B Bowden, John M Mendenhall, Wickliffe C Abraham, et al. Boundary learning by optimization with topological constraints. In *Computer Vision and Pattern Recognition (CVPR), 2010 IEEE Conference on*, pages 2488–2495. IEEE, 2010.

Shantanu H Joshi, Eric Klassen, Anuj Srivastava, and Ian Jermyn. Removing shape-preserving transformations in square-root elastic (SRE) framework for shape analysis of curves. In *Energy Minimization Methods in Computer Vision and Pattern Recognition*, pages 387–398. Springer, 2007.

Philipp Kainz, Michael Pfeiffer, and Martin Urschler. Semantic segmentation of colon glands with deep convolutional neural networks and total variation segmentation. *arXiv preprint arXiv:1511.06919*, 2015.

Alex Krizhevsky, Ilya Sutskever, and Geoffrey E Hinton. Imagenet classification with deep convolutional neural networks. In *Advances in Neural Information Processing Systems*, pages 1097–1105, 2012.

Yann LeCun, Koray Kavukcuoglu, and Clément Farabet. Convolutional networks and applications in vision. In *Circuits and Systems (ISCAS), Proceedings of 2010 IEEE International Symposium on*, pages 253–256. IEEE, 2010.

Jonathan Long, Evan Shelhamer, and Trevor Darrell. Fully convolutional networks for semantic segmentation. In *Proceedings of the IEEE Conference on Computer Vision and Pattern Recognition*, pages 3431–3440, 2015.

Maurice B Loughrey, Philip Quirke, and Neil A Shepherd. *Dataset for colorectal cancer histopathology reports, 3ed.* London: Royal College of Pathologists, 2014.

Jiri Matas, Ondrej Chum, Martin Urban, and Tomás Pajdla. Robust wide-baseline stereo from maximally stable extremal regions. *Image and Vision Computing*, 22(10): 761–767, 2004.

Bojana Mitrovic, David F Schaeffer, Robert H Riddell, and Richard Kirsch. Tumor budding in colorectal carcinoma: time to take notice. *Modern Pathology*, 25(10): 1315–1325, 2012.

Engin Ozdemir and Cigdem Gunduz-Demir. A hybrid classification model for digital pathology using structural and statistical pattern recognition. *Medical Imaging, IEEE Transactions on*, 32(2):474–483, 2013.

CH Richards, CSD Roxburgh, JH Anderson, RF McKee, AK Foulis, PG Horgan, and DC McMillan. Prognostic value of tumour necrosis and host inflammatory responses in colorectal cancer. *British Journal of Surgery*, 99(2):287–294, 2012.

Olaf Ronneberger, Philipp Fischer, and Thomas Brox. U-net: Convolutional networks for biomedical image segmentation. In Nassir Navab, Joachim Hornegger, WilliamM. Wells, and AlejandroF. Frangi, editors, *Medical Image Computing and Computer-Assisted Intervention MICCAI 2015*, volume 9351 of *Lecture Notes in Computer Science*, pages 234–241. Springer International Publishing, 2015. ISBN 978-3-319-24573-7.

Raphael Rubin, David S Strayer, Emanuel Rubin, et al. *Rubin's pathology: clinicopathologic foundations of medicine.* Lippincott Williams & Wilkins, 2008.

Minalini Shanmugathasan and Serge Jothy. Apoptosis, anoikis and their relevance to the pathobiology of colon cancer. *Pathology International*, 50(4):273–279, 2000.

K. Sirinukunwattana, D.R.J. Snead, and N.M. Rajpoot. A stochastic polygons model for glandular structures in colon histology images. *Medical Imaging, IEEE Transactions on*, 34(11):2366–2378, Nov 2015. ISSN 0278-0062. doi: 10.1109/TMI.2015.2433900.

Ali Tabesh, Mikhail Teverovskiy, Ho-Yuen Pang, Vinay P Kumar, David Verbel, Angeliki Kotsianti, and Olivier Saidi. Multifeature prostate cancer diagnosis and Gleason grading of histological images. *Medical Imaging, IEEE Transactions on*, 26(10):1366–1378, 2007.

Joke Tommelein, Laurine Verset, Tom Boterberg, Pieter Demetter, Marc Bracke, and Olivier De Wever. Cancer-associated fibroblasts connect metastasis-promoting communication in colorectal cancer. *Frontiers in Oncology*, 5, 2015.

Mary Kay Washington, Jordan Berlin, Philip Branton, Lawrence J Burgart, David K Carter, Patrick L Fitzgibbons, Kevin Halling, Wendy Frankel, John Jessup, Sanjay Kakar, et al. Protocol for the examination of specimens from patients with primary carcinoma of the colon and rectum. *Archives of Pathology & Laboratory Medicine*, 133(10):1539, 2009.

H-S Wu, R Xu, N Harpaz, D Burstein, and J Gil. Segmentation of intestinal gland images with iterative region growing. *Journal of Microscopy*, 220(3):190–204, 2005a.

Hai-Shan Wu, Ruliang Xu, Noam Harpaz, David Burstein, and Joan Gil. Segmentation of microscopic images of small intestinal glands with directional 2-d filters. *Analytical and Quantitative Cytology and Histology/the International Academy of Cytology and American Society of Cytology*, 27(5):291–300, 2005b.

Laurent Younes. Computable elastic distances between shapes. *SIAM Journal on Applied Mathematics*, 58(2):565–586, 1998.

Yan Zhang, Bogdan J Matuszewski, Lik-Kwan Shark, and Christopher J Moore. Medical image segmentation using new hybrid level-set method. In *BioMedical Visualization, 2008. MEDIVIS'08. Fifth International Conference*, pages 71–76. IEEE, 2008.